HHS Public Access

Author manuscript

Biomaterials. Author manuscript; available in PMC 2019 October 01.

Published in final edited form as:

Biomaterials. 2018 October ; 181: 67–80. doi:10.1016/j.biomaterials.2018.07.037.

A biodegradable synthetic graft for small arteries matches the performance of autologous vein in rat carotid arteries

Kee-Won Lee[a], **Piyusha S. Gade**[a], **Liwei Dong**[b,1], **Zhaoxiang Zhang**[b,1], **Ali Mubin Aral**[c], **Jin Gao**[a], **Xiaochu Ding**[d], **Chelsea E.T. Stowell**[d], **Muhammad Umer Nisar**[e], **Kang Kim**[a,e,f,g], **Dieter P. Reinhardt**[h], **Mario G. Solari**[b], **Vijay S. Gorantla**[b,2], **Anne M. Robertson**[a,g,i], **Yadong Wang**[a,3,*]

[a]Department of Bioengineering, University of Pittsburgh, Pittsburgh, PA 15261, USA

[b]Department of Plastic Surgery, University of Pittsburgh Medical Center, Pittsburgh, PA 15261, USA

[c]Department of Surgery, University of Pittsburgh, Pittsburgh, PA 15260, USA

[d]Meinig School of Biomedical Engineering, Cornell University, Ithaca, NY 14853, USA

[e]Center for Ultrasound Molecular Imaging and Therapeutics, Department of Medicine, University of Pittsburgh School of Medicine, Pittsburgh, PA 15213, USA

[f]Heart and Vascular Institute, University of Pittsburgh Medical Center, Pittsburgh, PA 15213, USA

[g]McGowan Institute for Regenerative Medicine, University of Pittsburgh, Pittsburgh, PA 15260, USA

[h]Faculty of Medicine, Department of Anatomy and Cell Biology, and Faculty of Dentistry, McGill University, Montreal, Quebec H3 A 0C7, Canada

[i]Department of Mechanical Engineering and Materials Science, University of Pittsburgh, Pittsburgh, PA 15261, USA

Abstract

Autologous veins are the most widely used grafts for bypassing small arteries in coronary and peripheral arterial occlusive diseases. However, they have limited availability and cause donor-site morbidity. Here, we report a direct comparison of acellular biodegradable synthetic grafts and autologous veins as interposition grafts of rat carotid arteries, which is a good model for clinically

[*]Corresponding author: Yadong Wang, Meinig School of Biomedical Engineering, Cornell University, 277 Kimball Hall, Ithaca, NY 14853, Phone: 607-255-4030; Fax: 607-255-7330; yw839@cornell.edu.

[1]Present address: Department of Plastic Surgery, Xijing Hospital, Fourth Military Medical University, Xi'an, Shaanxi, 710032, China

[2]Present address: Departments of Surgery, Ophthalmology and Bioengineering, Wake Forest Baptist Medical Center, Wake Forest Institute for Regenerative Medicine, Winston-Salem, NC, 27101, USA

[3]Present address: Meinig School of Biomedical Engineering, Cornell University, Ithaca, NY 14853, USA

Disclosures

The authors declare no competing financial interests.

Supplementary materials

Supplementary materials (Supplementary Table S1 and Fig.S1 – S9) related to this article are provided as a separate file.

Data availability

All data generated and analyzed during the current study are available from the corresponding author on reasonable request.

relevant small arteries. Notably, extensive but transient infiltration of circulating monocytes at day 14 in synthetic grafts leads to a quickly-resolved inflammation and arterial-like tissue remodeling. The vein graft exhibits a similar inflammation phase except the prolonged presence of inflammatory monocytes. The walls of the remodeled synthetic graft contain many circumferentially aligned contractile non-proliferative smooth muscle cells (SMCs), collagen and elastin. In contrast, the walls of the vein grafts contain disorganized proliferating SMCs and thicken over time, suggesting the onset of stenosis. At 3 months, both grafts have a similar patency, extracellular matrix composition, and mechanical properties. Furthermore, synthetic grafts exhibit recruitment and re-orientation of newly synthesized collagen fibers upon mechanical loading. To our knowledge, this is the first demonstration of a biodegradable synthetic vascular graft with a performance similar to an autologous vein in small artery grafting.

Keywords

Blood vessels; Autologous vein; Vascular grafts; Tissue engineering; Poly(glycerol sebacate)

1. Introduction

The need for small-diameter vascular grafts increases with the high incidence of vascular occlusive diseases. Although endovascular interventions are appropriate for some patients, bypass grafting is routinely performed for longer-term revascularization or when stents fail [1]. For bypassing small-diameter (< 6 mm) arteries, the saphenous vein is commonly used because it is easily harvested, and more readily available than arteries [2]. Vein grafts are implanted to bypass approximately 250,000 coronary and 80,000 lower extremity arteries in the United States annually [3]. However, autologous veins have limited availability and cause significant donor-site morbidity [4, 5]. Tissue engineering may provide an arterial substitute and has shown promising results in low pressure or high flow systems but requires isolation, seeding and culturing of human cells [6–9].

We set out to design a synthetic graft that can withstand arterial pressure immediately upon implantation and leverage the natural regenerative capabilities of the host to transform the structure into an arterial conduit *in vivo*, bypassing cell harvesting and culture completely. We use a relatively fast-degrading and highly porous tube as the major component [10] to enable rapid cell infiltration and host remodeling. The polymer, poly(glycerol sebacate) (PGS), is elastomeric and promotes elastin synthesis [11]. The tubular core is surrounded by a slow-degrading and thin sheath made of poly(caprolactone) (PCL) to increase suturability and avoid graft dilation. Multi-layered and bi-layered designs have been previously reported in tissue engineered vascular structures made of collagen gels [12], poly(ester urethane)urea [13], and PCL micro and nanofibers [14, 15]. The composition of our bi-layered graft is different in that > 90% of the graft is made of PGS. This design induces the host to replace the acellular scaffold with a structurally sound vascular conduit in a rat abdominal aorta at 3 months [10] and further matched the elastin content while maintaining good patency in a 1-year follow-up [16]. Recent studies using the fast-degrading material support our approach, demonstrating cell infiltration and vascular remodeling and inhibited calcification in mouse and rat aorta [17, 18]. However, the aorta is a large-diameter artery with a high blood flow

and its hemodynamics and mechanical properties are quite different from small-diameter arteries. The small diameter increases the risk of early graft stenosis and thrombosis [19, 20] and the low blood flow affects long-term patency of the grafts [21]. Thus, we examined whether our design would meet the more stringent requirement of grafting rat carotid arteries. Furthermore, we compared the performance with the autologous graft from external jugular veins because the vein is the largest source for small artery grafting clinically.

Previous studies of degradable synthetic grafts in small arteries have used the common carotid artery because it is easily accessible and long enough to implant and monitor the graft [22]. Compared to the aorta, the common carotid has a smaller diameter, lower blood flow and is more muscular and stiffer. Acellular grafts made of PCL and chitosan enhances cell infiltration and arterial remodeling in carotid arteries and supports the feasibility of using synthetic grafts in the peripheral arterial circulation [23]. However, the presence of significant graft materials at the terminal time point makes it difficult to predict outcome upon complete degradation of the graft material. We chose 3 months as a terminal time point for this study because very little graft material is left and the remodeled conduit consists mostly of host tissues. The key data are patency, morphological change, inflammatory responses, cellular organizations, extracellular matrix (ECM) production, and mechanical properties.

2. Materials and Methods

2.1. Fabrication of grafts

PGS prepolymer was synthesized in-house as described previously [24]. The PGS core was fabricated from a solvent casting and salt leaching method using 25-32 μm grounded salts as porogens, a stainless steel rod (outer diameter = 0.8 mm) as a mandrel, and a Teflon® tube (inner diameter = 1.58 mm, length = 20 mm) as a mold [25]. To fabricate the outer sheath, PCL (M_n = 80,000 Da) (Sigma-Aldrich, St. Louis, MO) was dissolved in 2,2,2-trifluoroethanol (ThermoFisher Scientific, Waltham, MA) at 14 weight/volume % and electrospun onto the rotating cured PGS-salt tubes using the following conditions: applied voltage = ± 12 kV, needle size = 22 gauge, distance between the needle and aluminum collector = 30 cm, distance between the mandrel and aluminium collector = 10 cm, infusion rate = 29 μl/min, and mandrel rotating speed = 80 rpm.

The thickness of PCL outer sheath was controlled in a targeted range of 20-25 μm by varying time and monitored using a high-speed laser micrometer (LS-7070M, Keyence Corp., Itasca, IL)

After electrospinning, PGS-PCL-salt tubes were dried in a vacuum chamber for 24 h and residual salt was dissolved in a series of two 10 mL water baths (first bath for 24 h and second bath for 48 h). Final grafts were lyophilized, sterilized with a gamma irradiation (dose = 25 kGy), and soaked into the heparin solution (100 U/mg) for 5 min before implantation.

2.2. Characterization of synthetic grafts

Gel permeation chromatography (GPC).—The molecular weights of the electrospun PCL sheets before and after gamma irradiation were examined using Waters Ambient Temperature GPC equipped with Gramm column and tetrahydrofuran (THF) as stationary and mobile phases (Waters Corporation, Milford, MA). Three different locations of the PCL sheets and the gamma-irradiated PCL sheets were taken for GPC analysis. The samples were prepared in THF at 1.5 mg/ml and filtrated through 0.2 μm syringe filter before the test (n = 3). Polystyrene was used as the standard polymer to calibrate the molecular weight.

Differential scanning calorimetry (DSC).—The crystallinity of electrospun PCL was measured before and after gamma sterilization. Five-milligram portions (n = 3) were scanned in a Q1000 MDSC (TA Instruments, New Castle, DE) operating in unmodulated mode. Samples were heated at 10°C/min from 25°C to 100°C. Crystallinity (X_c) was calculated as:

$$X_c = \frac{\Delta H_f}{\Delta H_f^\circ}$$

where ΔH_f is the measured heat of fusion and ΔH_f° is the heat of fusion of purely crystalline PCL, taken as 136 J/g [26].

Uniaxial tensile test.—Electrospun PCL sheets before and after gamma sterilization were cut using the dog-bone cutting die (TestResources Inc., Shakopee, MN). The mechanical properties were measured according to the standard method (ASTM D412) using an electromechanical testing machine (Insight, MTS Systems, Eden Prairie, MN) equipped with a 5 N load cell. Uniaxial tensile force was applied to dog-bone samples (n = 3; overall length = 28 mm, overall width = 5 mm, gauge length = 7 mm, and width of narrow section = 1 mm) at a rate of 5 mm/min with recording the force until failure. Ultimate tensile stress, linear elastic modulus, and strain at break were calculated from the stress-strain curve.

Scanning electron microscopy (SEM).—The morphology of the synthetic grafts was examined using SEM. Grafts were cut into 2 mm segments transversely, mounted onto aluminum stubs, sputter-coated with gold, and observed with a field emission SEM (6330F, JEOL, Tokyo, Japan). Inner diameter, wall, and PCL sheath thicknesses of the graft were measured from cross-sectional SEM images using ImageJ software (National Institutes of Health (NIH), Bethesda, MD).

X-ray micro-computed tomography.—Porosity and pore size distribution of grafts were measured using X-ray micro-computed tomography (micro-CT) as described previously [27]. Grafts (10-mm long) were mounted in styrofoam tubes affixed to a brass stub and scanned using the submicron (0.35 μm) resolution micro-CT (Skyscan 1272, Bruker Corp., Billerica, MA) with the following settings: average camera pixel size = 7.4 μm, image pixel size = 2.53 μm, frame averaging of 10, rotation step size of 0.1 degrees, scanned 180 degrees around the vertical axis. Three-dimensional (3D) images were reconstructed as a stack of 2.53 μm thick sections in the axial plane using the reconstruction

software (NRecon, Bruker Corp.). Total porosity and pore size distribution were calculated using the morphometric analysis software (CTAn, Bruker Corp.) by thresholding the sample in the region of interest followed by despeckling and 3D analysis. Pore interconnectivity was assessed by binarizing the solid strut and pore spaces, eliminating any disconnected closed pores, determining the scaffold and open pore volume, and calculating the ratio of this open pore volume to total pore volume, where open pore volume is the volume of black voxels within a solid (white) object that has a connection in 3D.

2.3. Animals and implantation of grafts

All procedures involving animals were approved by the Institutional Animal Care and Use Committee at the University of Pittsburgh following NIH guidelines for the care and use of laboratory animals. Male Sprague Dawley rats (8 to 9 weeks old; 225-250 g, $n = 50$, Charles River Laboratories, Wilmington, MA) were used in this study. Eight rats were used to characterize carotids and external jugular veins ($n = 4$ each) for cell and ECM content and dimensions. For graft implantation, 42 rats were randomly divided into two groups: synthetic grafts and autologous vein grafts. The 21 rats in each group were randomly divided into 7 rats for each time point (day 14, 30, and 90), selected based on our previous study demonstrating near complete graft material degradation within 90 days [10].

Rats were anesthetized with isoflurane inhalation (5% for induction, then 1-3% for maintenance), and their limbs were fixed in the supine position.

Experimental group: The midline of the neck was cut longitudinally. Blunt dissection created the operating space, exposing left sternocleidomastoid and sternohyoid. The left sternocleidomastoid was retracted to the lateral side, then the left common carotid artery was exposed, clamped, and transected it at 2 mm proximal to the bifurcation of internal and external carotid artery; a segment of 5 mm common carotid artery was removed as well. The graft (10-mm long) was interpositioned by end-to-end anastomosis using interrupted 10-0 polyamide monofilament sutures (AROSurgical, Newport Beach, CA).

Control group: To compare with synthetic grafts, the autologous external jugular vein was used as a control. The skin incision was made in the same way as described above. The left external jugular vein was exposed, ligated all branches, and harvested as 10-mm long segment. The left common carotid artery of the same rat was exposed, clamped, and transected as mentioned above. The external jugular vein was interpositioned by end-to-end anastomosis using running 10-0 polyamide monofilament sutures. No anti coagulation and antiplatelet treatments were administrated during and after implantation. The contralateral right common carotid artery was used as an age-matched healthy control. Both antibiotic (Baytril, 10 mg/kg) and analgesic (Buprenorphine, 0.1 mg/kg) medications were given until 72 h after implantation. To measure dimensions of native vessels, native common carotid arteries and external jugular veins ($n = 4$ each) were explanted, cut as 2-mm thickness, and viewed with a stereomicroscope (SMZ745T, Nikon Instruments Inc., Melville, NY). Both inner diameter and wall thickness were measured from cross-sectional images using the NIS-Elements software (Nikon).

2.4. Patency monitoring with ultrasonography

The blood flow was checked with a flow coupler monitor (GEM1020M, Synovis Micro, Birmingham, AL) at 5, 10, 15, and 30 min after removing clamps. A high-frequency ultrasound imaging system (Vevo2100, FUJIFILM Visualsonics, Toronto, Canada) was used to monitor the inner diameter and flow velocity of mid-grafts and contralateral native carotids at day 14, 30, 60 and 90 after implantation. Animals were anesthetized with 1-2% isoflurane via precision vaporizer and 1 L per minute gas flow and placed on a custom-built platform with a warming pad in a position. The hair on the neck area was removed with hair removal cream and ultrasound gel (AccuGel, Lynn Medical, Wixom, MI) was then applied to the skin. Transcutaneous ultrasound imaging was performed on the neck using a linear array transducer MS 550 centered at 40 MHz. B-mode, color Doppler mode, and PW mode images along the long axis and middle region of the graft and native carotids were measured through the cardiac cycle recorded from ECG leads and stored for offline analysis. Cine loop images were later analyzed using a high-frequency ultrasound imaging system (Vevo2100) software for overall patency, inner diameter changes, and flow velocity at and around the graft. Both the inner diameter and flow velocity were obtained by averaging end-diastolic and end-systolic inner diameter and flow velocity measured from B-mode and PW mode images, respectively.

2.5. Histology and morphometrical analysis

All explanted grafts and native carotids were rinsed with PBS, fixed in 10% formalin for 1 h at 4°C, and dehydrated in 30% sucrose solution at 4°C for 24 h. Tissue sections were embedded in optimal cutting temperature compound (Sakura Finetek, Torrance, CA), frozen at −80°C for 2 h, and cryosectioned to 8-μm thickness. Tissue slides were stained with H&E, Masson's trichrome, Verhoeff-van Gieson, and Alizarin red to examine cell presence and infiltration, collagen, elastin, calcium, respectively. All histological images were representative of three independent sections per group ($n = 4$) and captured with an inverted microscope (Eclipse Ti-E, Nikon). The luminal area and wall thickness of both grafts and native carotids were measured from H&E staining images with a high-power magnification (60×) using the NIS-Elements software (Nikon).

2.6. Immunofluorescence staining

Tissue sections (8-μm thick) were fixed with 4% paraformaldehyde for 1 h at 4°C and permeabilized with 0.2% Triton X-100 for 5 min at room temperature. Tissue sites on slides were blocked with 5% normal goat serum (NGS) (Sigma-Aldrich) for 24 h at 4°C, incubated with primary antibodies in 1% NGS for 45 min at 37°C, were rinsed twice with PBS, followed with the corresponding secondary antibodies in 1% NGS for 45 min at 37°C. Antibodies used are described in Table S1. Nuclei were counterstained with 4′,6-diamidino-2-phenylindole (DAPI) (Life Technologies, Carlsbad, CA) at room temperature for 20 min. Tissue slides without primary antibodies were used as negative controls.

2.7. Counting of immunofluorescent-positive inflammatory cells

Slides stained with inflammatory cell markers were viewed under high-power magnification (60×) and four randomly selected regions of interests (ROIs) were captured with the inverted

microscope. Images were representative of three independent sections per graft ($n = 4$) and analyzed by a blinded investigator. The area size of the positive fluorescent signal within four ROI images was quantified, summed, and averaged for each sample using the NIS-Elements software. The area size of total cells within four ROI images was assessed by DAPI staining. The total number of immunofluorescent-positive cells in each sample was calculated as (the area size of the positive staining for each marker / the area size of DAPI positive staining) × 100 and expressed as a percentage of the area.

2.8. Endothelial cell examination at the lumen

The grafts and native carotids were explanted at day 90, cut longitudinally by using microscissors, and fixed with minute pins. For SEM, samples were fixed with 2.5% glutaraldehyde for 2 h at room temperature, washed with PBS, and dehydrated in graded series of ethanol. After the critical-point drying, samples were mounted on aluminum stubs, sputter-coated with gold, and observed with a field emission SEM. For en face immunofluorescence staining, samples were fixed with 4% paraformaldehyde at 1 h and permeabilized with 0.2% Triton X-100 for 5 min at room temperature. Samples were blocked with 5% NGS for 24 h at 4°C, incubated with the mouse anti-CD31 (1:200, Abeam, Cambridge, MA) primary antibody, and then incubated with Alexa Fluor 594 goat anti-mouse IgG (1:400) secondary antibody. Immunofluorescence images were captured with the inverted microscope.

2.9. Western blot analysis

The grafts and native carotids were homogenized in cold RIPA buffer (Cell Signaling Technology, Danvers, MA) containing protease inhibitor cocktail. The homogenized tissues were centrifuged at 14,000×g for 10 min at 4°C and protein contents of the supernatants were measured by Pierce 660nm Protein Assay (ThermoFisher Scientific). Equal amounts (20 μg) of proteins were separated on 8% SDS/PAGE gels and transferred onto polyvinylidene fluoride membranes (ThermoFisher Scientific). Membranes were blocked with 5% bovine serum albumin (EMD Millipore, Burlington, MA) and incubated with primary antibodies at 4°C with shaking at 90 rpm overnight. After washing with Tris-buffered saline, membranes were probed with secondary antibodies at room temperature for 2 h. Antibodies used are described in Table S1. HRP-based detection was performed using Pierce ECL Western Blotting Substrate (ThermoFisher Scientific). Membranes were stripped and reprobed, and blots were visualized by X-ray film exposure with the use of a quality X-ray processor (AX700LE, Alphatek, Salem, WI). The intensity of blots was quantified using ImageJ software (NIH) and normalized to that of β-actin.

2.10. Biochemical assays

Collagen quantification.—Collagen contents of grafts and native carotids were measured using the Sircol Insoluble Collagen Assay kit (Accurate Chemical & Scientific Corp., Westbury, NY). Tissue segments (3-mm long) were minced finely, weighed to obtain wet weight, and then digested with the Fragmentation Reagent at 65 °C for 2 h 30 min to convert the insoluble collagen to denatured soluble collagen. Collagen content in pooled

supernatants was measured following the manufacturer's instructions and normalized to tissue wet weight (μg/mg).

Elastin quantification.—Elastin contents of grafts and native carotids were measured using a Fastin Elastin Assay kit (Accurate Chemical & Scientific Corp.). Tissue segments (3-mm long) were minced finely, weighed to obtain wet weight, and then digested with 0.25M oxalic acid at 100 °C for 1 h three times to extract the mature insoluble elastin into the solution supernatant. Elastin content in pooled supernatants was measured following the manufacturer's instructions and normalized to tissue wet weight (μg/mg). The sample size was $n = 4$ for graft explants and native carotids. All samples were tested in triplicate during the same assay run. Bare synthetic grafts were used as a negative control.

2.11. Mechanical evaluation

Suture retention strength measurement.—Suture retention strength of grafts and native vessels was measured using an electromechanical testing machine (Insight, MTS Systems) equipped with a 5 N load cell according to ISO 7198. Both bare grafts and explanted external jugular veins and native carotids were cut longitudinally by microscissors to obtain rectangular samples (length = 10 mm, width = 4 mm). A single 9-0 Nylon suture (AROSurgical) was inserted through the 2 mm of the edge of each sample and tied to form a loop. The non-sutured end of each sample and the suture loop were secured to separate clamps in the testing machine and the suture was pulled at the rate of 50 mm/min with recording the force. Both grafts and native vessels were tested in the wet state using saline at room temperature. Suture retention strength was defined as the maximum force recorded before the suture was pulled through each sample. The sample size was $n = 5$ for grafts and native vessels.

Biaxial inflation test.—Circumferential mechanical properties of the explanted grafts were measured using a custom-designed biaxial inflation testing device. Entire segments of grafts were mounted on the device by suturing them on cannulae and immersed in a water bath maintained at 37°C. 350-400 μm microspheres (Zephyrtronics Inc., Pomona, CA) were lightly glued on the surface of grafts and tracked using a video camera (EO-5012C, Edmund Optics, Barrington, NJ) which captures images at 5 megapixels and 6 frames per second giving a final pixel size of 2.2 × 2.2 μm to obtain local axial strain measurement. Both axial and circumferential strains were calculated by analyzing these images using a custom code in MATLAB (R2014b, Mathworks, Natick, MA). The load was measured using a high precision load cell (MDB-5, Transducer Techniques, Temecula, CA) mounted on one end of the device and axial strain controlled using a computer controlled actuator (ANT-25LA, Aerotech Inc., Pittsburgh, PA). Testing consisted of four preconditioning cycles during which the grafts were stretched to the *in vivo* axial strain level and cycled from 0-120 mmHg. Following preconditioning, the grafts were tested at the following axial strain levels: 0, 10, 20%, *in vivo* strain and 40% axial strains by performing three inflation cycles from 0-120 mmHg at each strain level. High-strain modulus was calculated by fitting a line to the high strain region of the stress-stretch curve with an $R^2 > 0.98$. Compliance was calculated as

$$C\ (\%/100mmHg) = \frac{\Delta D}{D_0}/\Delta P$$

Where ΔD is the change in the inner diameter of the sample. The outer diameter is measured and thickness calculated using the isovolumetric deformation assumption. D_0 is the inner diameter at 70 mmHg and ΔP is 40 mmHg.

Burst pressure measurement.—Explanted grafts and native carotids (10-mm long, n = 3 each) were cannulated and pressurized with PBS using 20 mL syringe at an infusion rate of 5 mL/min until failure. The luminal pressure was measured using a pressure transducer (PX309-100G5V, Omega Engineering Inc., Stamford, CT) with a range of 0-5000 mmHg. The data were recorded using a data acquisition system (PowerLab 8/30, ADInstruments, Colorado Springs, CO).

Collagen fiber imaging at biaxial loads.—Explanted grafts and native carotids (10 mm long, n = 3 each) were cannulated and mounted on the biaxial inflating testing device. The device was then mounted directly under a multiphoton microscope (FV1000 MPE, Olympus, Center Valley, PA) objective lens to image the vessel during various loading conditions. Specimens were axially stretched to their respective measured *in vivo* strains and imaged at two pressures; 0 mmHg (no load) and 120 mmHg (maximum physiologic load). An excitation wavelength of 800 nm and 1.12 NA 25× MPE water immersion objective was used for all samples. SHG signal was collected using a 400 nm emission filter with ± 50 spectral bin. Planar images were taken starting from the outer wall, moving toward lumen at 2 μm intervals. Collagen fiber recruitment was quantified through fiber tortuosity using the manual filament tracing function in Imaris (Bitplane, Switzerland). Fibers were manually traced on 2D images using superimposed projections of the 3D images across the thickness of the sample within a central region (200 × 100 μm) chosen such that it was possible to go through the thickness of the entire sample. A straightness value of 1 represents fully recruited collagen fibers and less than 1 represents crimped (wavy) fibers. Similarly, collagen fiber orientation was quantified using the manually traced fibers mentioned above. Angle θ = 0° and 90° represent fibers aligned in the circumferential and longitudinal direction, respectively.

2.12. Statistical analysis

All measured data were reported as a mean ± SD. A log-rank test (for survival curve) and an unpaired, two-tailed Student's *t*-test were performed to compare two groups. A one-way analysis of variance (ANOVA) with Tukey's multiple comparisons was performed to compare three groups. Statistical analysis was performed using Prism version 7 (GraphPad Software, La Jolla, CA) to assess the statistical significance at $P < 0.05$.

3. Results

3.1. Graft characterization

SEM image of a representative synthetic graft showed the porous PGS core and the electrospun PCL sheath (Fig. S1A) with an inner diameter of 768 ± 24 μm matching that of the vein graft, and significantly larger than that of the native common carotid artery (referred to as a carotid) ($P = 0.0037$) (Fig. S1B). The wall thickness was 391 ± 23 μm, significantly larger than that of the carotid ($P < 0.0001$) and vein ($P = 0.0074$). The PCL sheath thickness was 23.6 ± 14 μm, matching in the targeted range (20-25 μm). Micro-computed tomography revealed a total porosity of 72.8 ± 1.9 % and the average pore size of 26.6 ± 3.2 μm, corresponding well to a calculated porosity of 75% and salt particles with diameters of 25-32 μm. Pore interconnectivity was > 99 %.

We assessed the effects of gamma irradiation on properties of the electrospun PCL outer sheath of synthetic graft using GPC, DSC, and uniaxial tensile test. GPC analyses demonstrated that gamma irradiation significantly reduced the weight average molecular weight (M_w) from 93,450 ± 1067 to 84,420 ± 1603 Da, a reduction of 9.7 ± 2.1 % ($P = 0.0094$) (Fig. S2A). However, the polydispersity (PDI) slightly increased from 1.363 ± 0.0291 to 1.404 ± 0.0216 after gamma irradiation without statistical difference ($P = 0.3218$) (Fig. S2B). The GPC spectra demonstrated a similarly narrow mass distribution with no traces of low molecular weight PCL being detected after the irradiation (Fig. S3). DSC analysis revealed that gamma irradiation did not significantly change crystallinity (44.9 ± 3.0 vs. 43.5 ±4.1 %, $P = 0.65$) (Fig. S4). Uniaxial tensile test demonstrated that gamma irradiation did not significantly affect UTS (24.6 ± 2.3 vs. 21.2 ± 2.0 MPa, $P = 0.067$) (Fig. S5A), linear elastic moduli (43.5 ± 3.6 vs. 37.7 ± 5.1 MPa, $P = 0.11$) (Fig. S5B), and strain at break (55.4 ± 2.1 vs. 52.0 ± 2.4 %, $P = 0.078$) (Fig. S5C).

3.2. Graft implantation and patency

We interpositioned both the synthetic and vein grafts ($n = 21$ each) in the left common carotid artery of Sprague Dawley rats and kept the right carotid as a control (Fig. 1A). Newly formed microvessels in the outer wall of both grafts suggested graft integration into the host. Ultrasonography at days 14, 30, 60, and 90 demonstrated open lumen and blood flow of the remodeled synthetic graft similar to those of vein grafts and the native common carotid artery (referred to as a “carotid” in all figures) at day 90 (Fig. 1B). The overall patency was 90.5% (19/21) for the synthetic grafts (referred to as “PGS-PCL” in all figures) and 100% (21/21) for vein grafts (“vein” in all the figures), and there was no statistical difference (Fig. 1C). One synthetic graft developed distal thrombosis at day 6 and one ruptured at day 9. The inner diameter of synthetic and vein grafts was similar but significantly larger than that of native carotids at all time points ($P < 0.05$) (Fig. 1D). At day 90, the inner diameter tended to be smaller in the vein graft (0.98 mm) than in the synthetic graft (1.13 mm), although this difference is statistically insignificant. The flow velocity of both grafts was similar to that of native carotids (contralateral) except that the vein graft displayed a significantly lower flow at day 14 ($P = 0.013$) (Fig. 1E). Thus, the synthetic grafts provided patency and stability equivalent to the vein at 3 months.

3.3. Histological and morphological assessments

We examined mid-sections of grafts using histology and morphometry to assess cell infiltration, organization, and morphological changes. H&E staining showed a substantial and early cell infiltration in synthetic grafts followed by cell and ECM organization (Fig. 2A). A dense luminal cell layer and little synthetic materials were visible in the wall at day 14. Cells distributed throughout the wall and were denser in the outer wall at day 30. Circumferentially-organized cells and ECM were observed in the wall with a distinct medial-like layer at day 90. The distribution of cells and ECM was asymmetric near the lumen but resembled native carotids. Conversely, vein grafts showed disrupted endothelium at the luminal surface, and cell infiltration from the outer wall at day 14, followed by increased cell density in the lumen at day 30. At day 90, dense and disorganized cells and ECM were observed within the inner wall.

Morphometrical analysis indicated that the luminal area increased gradually in synthetic grafts, but decreased in vein grafts with time (Fig. 2B). At days 14 and 30, there was no significant difference in the luminal area between the synthetic and vein grafts. However, the vein displayed a trend of decreasing luminal area and became significantly smaller than that of the synthetic graft at day 90 ($P = 0.036$). Both grafts had significantly larger luminal area and wall thickness than native carotids at all time points ($P < 0.001$). However, the wall thickness increased in vein grafts but decreased in synthetic grafts so the latter approached the thickness of native carotids over time while the former thickened (Fig. 2C).

Furthermore, while the synthetic grafts showed consistent luminal area and wall thickness throughout the graft at all time points, the vein graft showed the distinct change of both the luminal area and wall thickness along the graft at the early time point (Fig. 3A). At day 14, the luminal area of the vein graft was minimal at the proximal region and became significantly larger toward the distal region ($P = 0.008$, middle and 0.0003, distal) than that of the synthetic graft ($P = 0.007$, distal) (Fig. 3B). In contrast, the wall thickness of the vein graft was maximal at the proximal region and became significantly smaller toward the distal region ($P < 0.0001$, middle and distal) than that of the synthetic graft ($P < 0.0001$, middle and distal) (Fig. 3C). At day 90, vein grafts had a significantly smaller luminal area ($P < 0.0003$) but the thicker wall ($P < 0.002$) at anastomotic regions than synthetic grafts.

3.4. Infiltration of inflammatory monocytes

We evaluated monocyte infiltration into the grafts to assess the initial host response. We stained mid-section of grafts with C-C chemokine receptor type 2 (CCR2) and CD11b, markers for monocyte recruitment, adhesion, and migration [28, 29]. The expression of CCR2 and CD11b were highest at day 14 and decreased thereafter in both grafts (Fig. 4A **and** 4C). Many $CCR2^+$ cells infiltrated synthetic grafts at day 14, but were almost absent at day 30, and disappeared at day 90. $CD11b^+$ cells were dispersed through the wall at day 14 and limited to the abluminal area thereafter. Conversely, in vein grafts, $CCR2^+$ cells dispersed throughout the wall at day 14 and persisted at the lumen and the abluminal areas at day 90. Quantification of the fluorescent-positive cells revealed that the synthetic grafts had more $CCR2^+$ cells at day 14 ($P = 0.015$) but less at days 30 ($P = 0.0003$) and 90 ($P = 0.002$)

than vein grafts (Fig. 4B). On the other hand, more $CD11b^+$ cells were detected in the synthetic graft than the vein grafts at days 14 ($P = 0.033$) and 90 ($P = 0.009$) (Fig. 4D).

3.5. Macrophage infiltration and polarization

We stained mid-sections of grafts with CD68, inducible nitric oxide synthase (iNOS), and CD206, markers of the newly recruited, pro-inflammatory (Ml), and alternatively activated (M2) macrophages, respectively. Consistent with CD11b expression, both CD68 and iNOS expression were highest in the lumen at day 14, decreased markedly thereafter, and were limited to the abluminal area in both grafts (Fig. 5A **and** 5C). Synthetic grafts showed significantly more $CD68^+$ cells than vein grafts at day 14 ($P = 0.034$) (Fig. 5B). There was no significant difference in the $iNOS^+$ cells between synthetic and vein grafts at all time points (Fig 5D). Conversely, CD206 expression was minimal at day 14 and increased gradually with time (Fig. 5E). At day 14, $CD206^+$ cells in synthetic grafts were significantly less than that in vein grafts ($P < 0.0001$); however, no difference was observed at later time points (Fig. 5F). The ratio of $iNOS^+$ to $CD206^+$ cells was significantly higher in synthetic grafts than in vein grafts at day 14 ($P < 0.0001$) but showed no significant difference thereafter (Fig. 5G). These results show that synthetic grafts enabled early infiltration of the classically activated macrophages, followed by a phenotype switching to the alternatively activated macrophages.

3.6. Arterial-like tissue remodeling

We examined the luminal surface using SEM and immunofluorescence staining with EC markers CD31 and vWF to assess EC coverage. At day 14, no ECs appeared in the synthetic grafts. Vein grafts showed disrupted endothelium in the luminal surface. At day 30, ECs covered the luminal surface of both grafts as demonstrated by vWF expression (Fig. S6A). SEM images showed that ECs completely covered the lumen of both grafts at day 90 and were aligned in the flow direction, resembling that of native carotids (Fig. S6B). Tightly-bound ECs with cobblestone-like morphology were clearly observed in synthetic grafts. $CD31^+$ and vWF^+ cells in the luminal surface confirmed EC coverage in both grafts (Fig. 6A). Western blot analysis indicated that both the remodeled synthetic and vein grafts expressed endothelial nitric oxide synthase (eNOS) and thrombomodulin (TM), but did not express vascular cell adhesion protein-1 (VCAM-1) and intercellular adhesion molecule-1 (ICAM-1), indicating quiescence (Fig. 6B). There were no significant differences in eNOS and TM expressions between the remodeled synthetic and vein grafts ($P = 0.98$ and 0.50) (Fig. 6C). However, eNOS and TM expressions in both grafts were significantly lower than in native carotids ($P < 0.05$).

We stained mid-section of grafts with smooth muscle contractile phenotypic and cell proliferating markers. Alpha-smooth muscle actin $(SMA)^+$ cells were observed in the middle of the wall at day 14 and dispersed at day 30 in both grafts. More αSMA^+ cells were organized near the outer layer of the remodeled synthetic grafts. In contrast, more αSMA^+ cells were present near the lumen of the vein grafts (Fig. S7). At day 90, the remodeled synthetic grafts showed a dense, concentric cell layer expressing calponin and myosin heavy chain, markers of contractile SMCs (Fig. 6D). There was no evidence of proliferating SMCs, indicated by a negative expression of Ki67. On the contrary, vein grafts contained numerous

proliferating αSMA$^+$ and Ki67$^+$ cells near the lumen. Alpha-SMA$^+$ cells were disorganized in the wall and the expression of calponin and myosin heavy chain was weaker than the remodeled synthetic grafts. We further investigated the activation of Akt and extracellular signal-regulated kinases 1 and 2 (ERK1/2) (Fig. 6E). These are protein kinases of phosphatidylinositol 3-kinase (PI3K)-Akt-mammalian target of rapamycin (mTOR) and Ras-mitogen-activated protein kinase (MAPK) cascades, both of which are major signaling pathways of SMC proliferation [30–32]. Western blot analysis indicated that the expression of phosphorylated-Akt and ERK1/2 was significantly higher in the vein graft than in the synthetic graft ($P = 0.0036$ and 0.0072) and native carotids ($P = 0.0008$ and 0.016) at day 90 (Fig. 6F). These results correlated with more proliferative SMCs in the vein graft at day 90. Taken together, the host remodeled synthetic grafts closer to native carotids than autologous vein grafts in terms of SMC phenotype and organization.

3.7. ECM protein deposition

ECM proteins provide mechanical support for the vessel and guide cellular differentiation and functions. We examined collagen and elastin using histology, immunofluorescence staining, and multiphoton microscopy. Masson's trichrome and Verhoeff-van Gieson staining showed collagen fibers spanning the wall and elastic fibers near the lumen in both grafts. Remodeled synthetic grafts had similar organization and distribution of ECM protein assemblies to native carotids with circumferentially organized collagen and elastin near the outer wall and the lumen, respectively. However, vein grafts had thick collagen fibers in the entire wall and aggregated elastin near the lumen. Alizarin red staining revealed that there is no calcification in either graft (Fig. 7A **and** S8). Immunofluorescence staining revealed the expression of collagen I and III across the entire wall. Furthermore, the remodeled synthetic grafts expressed elastin and fibrillin-1. Vein grafts displayed weaker expression of fibrillin-1 in the lumen than the remodeled synthetic grafts. Biochemical assays indicated that both grafts contained comparable quantities of collagen (Fig. 7B), but significantly less elastin than native carotids ($P < 0.0003$) (Fig. 7C). As implanted, the synthetic grafts contain no protein but have similar collagen and elastin contents to the vein graft at 3 months: these were 88% and 23% of those in native carotids, respectively.

3.8. Mechanical properties

We evaluated mechanical properties of grafts and native carotids using suture retention, biaxial inflation – extension (Fig. S9), compliance, and burst pressure tests. Suture retention strength of both bare grafts and explanted external jugular veins was similar ($P = 0.0505$), but significantly lower than that of native carotids ($P < 0.0001$ and 0.0024) (Fig. 8A). There was no significant difference in the mechanical performance of the two types of grafts; both lacked a toe-region leading to a lower range of stretch in the loading curves compared with native carotids. At physiological values of pressure, the intramural stress within both grafts was in the range of 40-50 kPa (Fig. 8B). Both grafts were significantly stiffer compared with native carotids as shown by the high strain modulus ($P = 0.031$) (Fig. 8C). There was no significant difference in the burst pressure, a marker of bulk strength, between all three groups (Fig. 8D), demonstrating that both types of grafts were capable of withstanding the arterial pressure by 3 months post-implantation. However, compliance of both grafts was significantly lower than that of native carotids ($P < 0.05$) (Fig. 8E).

We assessed the microstructural response to loading of each of the groups using second harmonic generation (SHG) imaging for collagen fibers and two-photon excitation for elastin fibers (Fig. 8F). The first main difference between the groups was the lack of visible elastin fibers in both grafts as compared to native carotids. Secondly, there was a difference in collagen fiber load bearing mechanism between the two grafts. In native carotids, collagen fibers bear biaxial load by two mechanisms – (a) recruitment (straightening) and (b) change in orientation (Fig. 8G). However, vein grafts did not exhibit collagen fiber recruitment or fiber re-alignment upon loading. Rather, most collagen fibers remained aligned in the axial (±60 - ±90°) direction and very few in the circumferential (−30 to +30°: 14% 0 mmHg vs. 16% 120 mmHg) direction upon pressurization. In contrast, 13% of collagen fibers in the remodeled synthetic graft were crimped under zero pressure and were recruited upon pressurization. Furthermore, fiber re-alignment measurements showed that remodeled synthetic grafts behaved similarly to native carotids with a significant ($P < 0.001$) change in fiber re-alignment upon pressurization. Fibers re-aligned from the longitudinal to the circumferential direction (−30 to +30°: 15% 0 mmHg vs 57% 120 mmHg) upon pressurization. These findings suggest that synthetic grafts enabled the remodeling of collagen fibers to bear biaxial load upon extension and pressurization.

4. Discussion

To date, all tissue-engineered grafts in clinical trials are cell-based, needing human cells for seeding polymeric scaffolds [7] or creating cell sheets [8]. Using banked allogeneic cells greatly reduces waiting time for grafts; however, isolation, expansion, and seeding of recipient endothelial or endothelial progenitor cells are still necessary. In a 1-month pig study, decellularized tissue-engineered matrix showed better patency rate than autologous internal jugular vein grafts, resisting luminal occlusion and intimal hyperplasia [33]. The dense collagenous matrix appears to inhibit host cell infiltration and ECM content was not reported. Decellularized porcine small intestine submucosa showed patency and arterial-like tissues similar to saphenous vein in a canine carotid model for 6 months [34]. However, this xenogeneic graft was prone to acute thrombosis, despite systemic administration of heparin. No ECM contents or mechanical data were reported.

The synthetic graft reported here relies on the host cells to infiltrate and remodel the synthetic grafts after implantation. Compared with autologous veins and current tissue-engineered grafts, these synthetic grafts avoid donor-site morbidity and immunogenicity, reduce fabrication cost and time, and ease storage and transport requirement. This approach poses its own challenges but offers the potential to combine the advantages of tissue-engineered grafts and conventional synthetic grafts.

We sterilized our vascular grafts by gamma irradiation using dosage of 25 kGy which is widely used for the medical devices [35]. Although the PCL sheath showed a significant reduction in M_w by the irradiation dosage (Fig. S2A), the sterilized PCL sheath still has molecular weight of 84,420 ± 1603 Da with a similarly narrow mass distribution (Fig. S2B). No traces of very low molecular weight PCL were generated by such a sterilization process according to the GPC analyses (Fig. S3). This is likely why we only observed mild, but not statistically significant, alterations on the material properties including the crystallinity,

UTS, elastic moduli and strain at break caused by the irradiation. A literature reported a dosage dependent effects on the properties of the electrospun PCL fibrous scaffolds by the gamma irradiation using a PCL with a similar molecular weight [36]. In our case, the property changes by the irradiation show a similar trend at the same dosage, but are much milder compared to the literature results. The fiber diameter and density by the electrospinning might be the other factors causing the discrepancy between our and the literature results.

Ultrasonography data indicated that the 90-day patency was similar for the synthetic and the autologous vein grafts. One synthetic graft developed a distal thrombosis at day 6 and one ruptured at day 9. Since the rupture was mainly due to a defect of the PGS core, we believe that defect-related failure will decrease significantly for larger and thicker grafts used in clinical applications and by the quality control steps in manufacturing. Compared with previous studies using acellular microfibrous grafts in the rat carotid artery interposition model, our grafts displayed a good patency at 90.5% without anti-thrombogenic surface modifications. Hirudin-polyethylene glycol (PEG) conjugated grafts showed 83% patency at 1 month and 86% patency at 6 months [37], and stromal cell-derived factor (SDF)-1α decorated grafts showed 89% patency at 3 months [38]. Despite the anti-thrombogenic surface modification, these results revealed that grafts with an inner diameter of 1 mm were prone to thrombosis. PCL grafts with an inner diameter of 0.7 mm also showed an overall 73% patency for 72 weeks but 57% patency for 12 weeks [39].

At 3 months, the autologous vein grafts showed certain signs of neointimal hyperplasia: reduced luminal area, thickened wall, and many proliferative SMCs in the wall. None of these were present in the remodeled synthetic grafts. Clinical data indicated that early geometrical changes were crucial determinants to long-term patency of vein grafts in bypass [40, 41]. Increased lumen and wall thickness in the vein graft in the first 1 month were usually followed by relative stability [42]. However, decreased lumen and increased wall thickness after 1 month generally indicated neointimal hyperplasia [43–47]. Initial lumen dilation of vein grafts was evidenced by maximal luminal area and minimal wall thickness at day 14. Additionally, vein grafts had lower flow velocity than carotids at day 14, but similar thereafter (Fig. 1E). This finding suggests that vein graft wall was still more distensible than the artery at early implantation and became stiffer with time. After day 14, the narrowing lumen and thickening wall reflected further adaptation processes with corresponding SMC migration and proliferation (Fig. S7 **and** 6D), and ECM deposition in the inner wall (Fig. 7A).

The divergence between the vein and the PGS-PCL grafts might be related to the different inflammatory responses. The PGS-PCL grafts induce more extensive early inflammatory response than vein grafts at day 14. There is no difference of M1 macrophages ($iNOS^+$) in both grafts. After 14 days, the population of pro-inflammatory cells subsides in the remodeled synthetic grafts, whereas M2 macrophages ($CD206^+$) increase. This finding suggests a resolution of inflammation and macrophage polarization towards a healing outcome. On the contrary, $CCR2^+$ cells persist to day 90 in vein grafts (Fig. 4A **and** 4B). CCR2, a monocyte chemoattractant protein (MCP)-l receptor, mediates monocyte migration from bone marrow to peripheral blood [48]. $CCR2^+$ cells, classified as inflammatory

monocytes [49], extravasate to inflamed tissues in the early inflammatory phase [28]. $CCR2^+$ cells enhance angiogenesis and tissue repair [50], however, excessive expression of MCP-1/CCR2 induces SMC proliferation, leading to intimal hyperplasia in vein grafts [51]. This is consistent with our observation of SMC proliferation and a narrower lumen in the vein graft at 90 days (Fig. 2B **and** 6D).

Short-term recruitment of bone marrow-derived circulating monocytes has been achieved in acellular grafts by a burst release of exogenous MCP-1 [52, 53]. Here, the graft design induces an initial influx of bone marrow-derived circulating monocytes, initiating inflammation-mediated vascular remodeling. $CD11b^+$ and $CD68^+$ cells remain near the abluminal surface of the synthetic grafts after day 14 (Fig. 4C **and** 5A). This could be caused by the continued presence of the small amount of PCL in the outer layer. Conversely, vein graft shows densely packed $CD11b^+$ and $CD68^+$ cells near both the luminal and abluminal surfaces at day 14, suggesting that living cells and ECM inhibit infiltration of these cells into the vessel wall. After day 14, $CD11b^+$ cells almost disappeared. It is likely that the slow degrading PCL sheath contributes to the extended presence of resident monocytes ($CCR2^-$, $CD11b^+$) [49] and their differentiation to tissue macrophages ($CD11b^+$, $CD68^+$) [54]. Tissue-resident macrophages have similar functions to M2 phenotypes that play a fundamental role in the resolution of inflammation and tissue homeostasis [55]. We found that both $CD68^+$ and $CD206^+$ but few $iNOS^+$ cells were observed in the same abluminal area in the remodeled synthetic grafts at day 90 (Fig. 5A, 5C, **and** 5E).

In the remodeled grafts, the distribution and organization of SMCs correlate directly with the morphology and organization of ECM proteins. Thick, disorganized collagen fibers and aggregated elastin are present in vein grafts alongside randomly orientated SMCs. On the other hand, the remodeled synthetic grafts have collagen and elastin aligned circumferentially alongside SMCs at 3 months, resembling the organization in native carotids (Fig. 7A). The newly synthesized elastin in the remodeled synthetic grafts co-exists with fibrillin-1 and is equivalent to 23% of that found in native carotids. Several studies have reported elastin production in small artery grafting using pre-clinical animal models. Decellularized engineered allografts contained elastin corresponded to 8.8% of an ovine femoral artery at 6 months [56]. Porcine small intestine submucosa grafts loaded with heparin and VEGF showed a varied range of elastin contents in an ovine carotid artery model at 3 months [57], but no fibrillar elastin was observed.

The functional requirements of replacement vascular grafts have changed from just sufficient suture retention strength and burst pressure to requiring functional adaptability and sound microstructure-function relationship. There is also a pressing need to understand the mechanical cues that govern ECM deposition and the manifestation of these cues into a structural response to gain a mechanistic understanding of the long-term graft remodeling. As the first step toward this, we used nondestructive SHG testing to understand the microstructural behavior of collagen loading. An important mechanism for compliance in the native arteries is the gradual recruitment and re-orientation of collagen fibers which leads to their nonlinear stress-strain relationship [58, 59]. At low loads, elastin fibers and the surrounding matrix are the main load-bearing components while collagen fibers are engaged at higher loads. While the origin of a crimp (waviness) in collagen fibers is unknown [60],

native arteries synthesize collagen at various levels of crimp. These undulations are one mechanism for enabling high compliance followed by stiffening at higher loads [61, 62]. In our remodeled synthetic grafts, some collagens exhibit crimp; however, most fibers are already straightened at low pressures (Fig. 8G), which is one of the main causes of a higher graft stiffness. This diminished crimp might be attributed to the fact that collagen fibers are being rapidly synthesized to bear load to compensate for the degradation of the graft material. Furthermore, as collagen fibers are continually turning over, it is possible that over a longer time frame, the level of crimp will increase.

We recognize that our synthetic grafts exhibited a significantly lower compliance at lower strains than that of native carotids (Fig. 8E), likely because of the low elastin content at 90 days. However, this does not inevitably preclude elastin synthesis at later timepoints as evidenced by comparable elastin production to the native aorta seen at 1 year in our previous work [16]. Thus, the lower compliance in our grafts than in native carotids is not necessarily a sign of maladaptive remodeling. Furthermore, collagen fibers in our grafts exhibit native-like functional behavior and are capable of recruitment and re-orientation during pressurization, suggesting that collagen is exhibiting adaptive remodeling. In contrast, vein grafts lack recruitment and re-orientation of collagen fibers upon loading which is more typical of scar-like collagen [63]. Consistent with the functional characteristics, histological and SHG imaging reveal thicker walls and dense collagen, which, coupled with high levels of proliferating SMCs, indicate a fibrotic remodeling response in the vein grafts. This work represents the first step towards a detailed mechanical and biological evaluation of remodeling grafts that requires a long-term study.

The observations in this study are limited to the rat model and the 3-month follow-up window. Rats enable a high-throughput, cost-effective study to assess cell infiltration [22]. However, rats have different regenerative potentials, hemodynamics, and physiology than humans. This study uses young rats; thus, the effect of aging on host remodeling remains unknown. To our knowledge, this is the first report of a synthetic graft that performs comparably to an autologous vein in small artery grafting. We are currently performing a long-term study in a sheep carotid model before the clinical translation of these grafts.

5. Conclusions

In summary, we developed biodegradable synthetic grafts that do not require cell seeding before implantation and compared their performance with autologous vein grafts in a rat carotid artery model for 3 months. Compared with autologous vein grafts, our synthetic grafts have: (1) similar patency without anti-thrombogenic surface modifications; (2) consistent morphological changes without any signs of stenosis; (3) extensive but transient infiltration of circulating inflammatory monocytes, leading to quickly-resolved inflammation and arterial-like tissue remodeling; (4) remodeled wall with circumferentially organized, contractile, non-proliferating SMCs; and (5) recruitment and re-orientation of newly synthesized collagen fibers upon mechanical loading. The critical next step of this study is to test our design in large animals and aged animals; both are currently under investigation.

Supplementary Material

Refer to Web version on PubMed Central for supplementary material.

Acknowledgments

We thank Xiaozhou Fan for assistance with ultrasonography, Dr. Michael W. Epperly for gamma sterilization, and Brandon B. Risley for assistance with GPC analysis. The GPC analysis made use of the Cornell Center for Materials Research Shared Facilities which are supported through the NSF MRSEC program (DMR-1719875). This work was supported by National Institutes of Health (R01HL089658 and 1R21HL124479-01). The small animal imaging system was supported by National Institutes of Health (1S10RR027383-01).

References

[1]. Antoniou GA, Chalmers N, Georgiadis GS, Lazarides MK, Antoniou SA, Serracino-Inglott F, Smyth JV, Murray D, A meta-analysis of endovascular versus surgical reconstruction of femoropopliteal arterial disease, J. Vase. Surg 57(1) (2013) 242–53.

[2]. de Vries MR, Simons KH, Jukema JW, Braun J, Quax PH, Vein graft failure: from pathophysiology to clinical outcomes, Nat. Rev. Cardiol 13(8) (2016) 451–70. [PubMed: 27194091]

[3]. Bhasin M, Huang Z, Pradhan-Nabzdyk L, Malek JY, LoGerfo PJ, Contreras M, Guthrie P, Csizmadia E, Andersen N, Kocher O, Ferran C, LoGerfo FW, Temporal network based analysis of cell specific vein graft transcriptome defines key pathways and hub genes in implantation injury, PLoS One 7(6) (2012) e39123. [PubMed: 22720046]

[4]. Athanasiou T, Saso S, Rao C, Vecht J, Grapsa J, Dunning J, Lemma M, Casula R, Radial artery versus saphenous vein conduits for coronary artery bypass surgery: forty years of competition—which conduit offers better patency? A systematic review and meta-analysis, Eur. J. Cardiothorac. Surg 40(1) (2011) 208–20. [PubMed: 21167726]

[5]. Harskamp RE, Lopes RD, Baisden CE, de Winter RJ, Alexander JH, Saphenous vein graft failure after coronary artery bypass surgery: pathophysiology, management, and future directions, Ann. Surg 257(5) (2013) 824–33. [PubMed: 23574989]

[6]. Shin'oka T, Imai Y, Ikada Y, Transplantation of a tissue-engineered pulmonary artery, N. Engl. J. Med 344(7) (2001) 532–3. [PubMed: 11221621]

[7]. Shin'oka T, Matsumura G, Hibino N, Naito Y, Watanabe M, Konuma T, Sakamoto T, Nagatsu M, Kurosawa H, Midterm clinical result of tissue-engineered vascular autografts seeded with autologous bone marrow cells, J. Thorac. Cardiovasc. Surg 129(6) (2005) 1330–8. [PubMed: 15942574]

[8]. L'Heureux N, McAllister TN, de la Fuente LM, Tissue-engineered blood vessel for adult arterial revascularization, N. Engl. J. Med 357(14) (2007) 1451–3. [PubMed: 17914054]

[9]. Lawson JH, Glickman MH, Ilzecki M, Jakimowicz T, Jaroszynski A, Peden EK, Pilgrim AJ, Prichard HL, Guziewicz M, Przywara S, Szmidt J, Turek J, Witkiewicz W, Zapotoczny N, Zubilewicz T, Niklason LE, Bioengineered human acellular vessels for dialysis access in patients with end-stage renal disease: two phase 2 single-arm trials, Lancet 387(10032) (2016) 2026–34. [PubMed: 27203778]

[10]. Wu W, Allen RA, Wang Y, Fast-degrading elastomer enables rapid remodeling of a cell-free synthetic graft into a neoartery, Nat. Med 18(7) (2012) 1148–53. [PubMed: 22729285]

[11]. Crapo PM, Wang Y, Physiologic compliance in engineered small-diameter arterial constructs based on an elastomeric substrate, Biomaterials 31(7) (2010) 1626–35. [PubMed: 19962188]

[12]. Weinberg CB, Bell E, A blood vessel model constructed from collagen and cultured vascular cells, Science 231(4736) (1986) 397–400. [PubMed: 2934816]

[13]. Nieponice A, Soletti L, Guan JJ, Hong Y, Gharaibeh B, Maul TM, Huard J, Wagner WR, Vorp DA, In Vivo Assessment of a Tissue-Engineered Vascular Graft Combining a Biodegradable Elastomeric Scaffold and Muscle-Derived Stem Cells in a Rat Model, Tissue Eng. Part A 16(4) (2010) 1215–1223. [PubMed: 19895206]

[14]. Nottelet B, Pektok E, Mandracchia D, Tille JC, Walpoth B, Gumy R, Moller M, Factorial design optimization and in vivo feasibility of poly(epsilon-caprolactone)-micro- and nanofiber-based small diameter vascular grafts, J. Biomed. Mater. Res. A 89(4) (2009) 865–75. [PubMed: 18465817]

[15]. de Valence S, Tille JC, Mugnai D, Mrowczynski W, Gurny R, Moller M, Walpoth BH, Long term performance of polycaprolactone vascular grafts in a rat abdominal aorta replacement model, Biomaterials 33(1) (2012) 38–47. [PubMed: 21940044]

[16]. Allen RA, Wu W, Yao M, Dutta D, Duan X, Bachman TN, Champion HC, Stolz DB, Robertson AM, Kim K, Isenberg JS, Wang Y, Nerve regeneration and elastin formation within poly(glycerol sebacate)-based synthetic arterial grafts one-year post-implantation in a rat model, Biomaterials 35(1) (2014) 165–73. [PubMed: 24119457]

[17]. Pan Y, Zhou X, Wei Y, Zhang Q, Wang T, Zhu M, Li W, Huang R, Liu R, Chen J, Fan G, Wang K, Kong D, Zhao Q, Small-diameter hybrid vascular grafts composed of polycaprolactone and polydioxanone fibers, Sci. Rep 7(1) (2017) 3615. [PubMed: 28620160]

[18]. Sugiura T, Tara S, Nakayama H, Yi T, Lee YU, Shoji T, Breuer CK, Shinoka T, Fast-degrading bioresorbable arterial vascular graft with high cellular infiltration inhibits calcification of the graft, J. Vase. Surg 66(1) (2017) 243–250.

[19]. Idu MM, Buth J, Hop WC, Cuypers P, van de Pavoordt ED, Tordoir JM, Factors influencing the development of vein-graft stenosis and their significance for clinical management, Eur. J. Vase. Endovasc. Surg 17(1) (1999) 15–21.

[20]. Schanzer A, Hevelone N, Owens CD, Belkin M, Bandyk DF, Clowes AW, Moneta GL, Conte MS, Technical factors affecting autogenous vein graft failure: observations from a large multicenter trial, J. Vase. Surg 46(6) (2007) 1180–90; discussion 1190.

[21]. Conte MS, The ideal small arterial substitute: a search for the Holy Grail?, FASEB J 12(1) (1998) 43–5. [PubMed: 9438409]

[22]. Swartz DD, Andreadis ST, Animal models for vascular tissue-engineering, Curr. Opin. Biotechnol 24(5) (2013) 916–25. [PubMed: 23769861]

[23]. Fukunishi T, Best CA, Sugiura T, Shoji T, Yi T, Udelsman B, Ohst D, Ong CS, Zhang H, Shinoka T, Breuer CK, Johnson J, Hibino N, Tissue-Engineered Small Diameter Arterial Vascular Grafts from Cell-Free Nanofiber PCL/Chitosan Scaffolds in a Sheep Model, PLoS One 11(7) (2016) e0158555. [PubMed: 27467821]

[24]. Wang Y, Ameer GA, Sheppard BJ, Langer R, A tough biodegradable elastomer, Nat. Biotechnol 20(6) (2002) 602–6. [PubMed: 12042865]

[25]. Lee SH, Lee KW, Gade PS, Robertson AM, Wang Y, Microwave-assisted facile fabrication of porous poly (glycerol sebacate) scaffolds, J. Biomater. Sci. Polym. Ed (2017) 1–19.

[26]. Tiptipakorn S, Keungputpong N, Phothiphiphit S, Rimdusit S, Effects of polycaprolactone molecular weights on thermal and mechanical properties of polybenzoxazine, J. Appl. Polym. Sci 132(18) (2015).

[27]. Gade PS, Lee K, Pfaff BN, Wang Y, Robertson AM, Degradation and erosion mechanisms of bioresorbable porous acellular vascular grafts: an in vitro investigation, J. R. Soc. Interface 14(132) (2017).

[28]. Shi C, Pamer EG, Monocyte recruitment during infection and inflammation, Nat. Rev. Immunol 11(11) (2011) 762–74. [PubMed: 21984070]

[29]. Solovjov DA, Pluskota E, Plow EF, Distinct roles for the alpha and beta subunits in the functions of integrin alphaMbeta2, J. Biol. Chem 280(2) (2005) 1336–45. [PubMed: 15485828]

[30]. Kingsley K, Huff JL, Rust WL, Carroll K, Martinez AM, Fitchmun M, Plopper GE, ERK1/2 mediates PDGF-BB stimulated vascular smooth muscle cell proliferation and migration on laminin-5, Biochem. Biophys. Res. Commun 293(3) (2002) 1000–6. [PubMed: 12051759]

[31]. Stabile E, Zhou YF, Saji M, Castagna M, Shou M, Kinnaird TD, Baffour R, Ringel MD, Epstein SE, Fuchs S, Akt controls vascular smooth muscle cell proliferation in vitro and in vivo by delaying Gl/S exit, Circ. Res 93(11) (2003) 1059–65. [PubMed: 14605018]

[32]. Muto A, Fitzgerald TN, Pimiento JM, Maloney SP, Teso D, Paszkowiak JJ, Westvik TS, Kudo FA, Nishibe T, Dardik A, Smooth muscle cell signal transduction: implications of vascular biology for vascular surgeons, J. Vase. Surg 45 Suppl A (2007) A15–24.

[33]. Quint C, Kondo Y, Manson RJ, Lawson JH, Dardik A, Niklason LE, Decellularized tissue-engineered blood vessel as an arterial conduit, Proc. Natl. Acad. Sci. USA 108(22) (2011) 9214–9. [PubMed: 21571635]

[34]. Sandusky GE Jr., Badylak SF, Morff RJ, Johnson WD, Lantz G, Histologic findings after in vivo placement of small intestine submucosal vascular grafts and saphenous vein grafts in the carotid artery in dogs, Am. J. Pathol 140(2) (1992) 317–24. [PubMed: 1739125]

[35]. Richards S, EN 552: validating 25 kGy as a sterilization dose, Med. Device Technol 7(6) (1996) 22–5.

[36]. Bosworth LA, Gibb A, Downes S, Gamma irradiation of electrospun poly(ε-caprolactone) fibers affects material properties but not cell response, J. Polym. Sci. B Polym. Phys 50(12) (2012) 870–876.

[37]. Hashi CK, Derugin N, Janairo RR, Lee R, Schultz D, Lotz J, Li S, Antithrombogenic modification of small-diameter microfibrous vascular grafts, Arterioscler. Thromb. Vase. Biol 30(8) (2010) 1621–7.

[38]. Yu J, Wang A, Tang Z, Henry J, Li-Ping Lee B, Zhu Y, Yuan F, Huang F, Li S, The effect of stromal cell-derived factor-1 alpha/heparin coating of biodegradable vascular grafts on the recruitment of both endothelial and smooth muscle progenitor cells for accelerated regeneration, Biomaterials 33(32) (2012) 8062–74. [PubMed: 22884813]

[39]. Kuwabara F, Narita Y, Yamawaki-Ogata A, Satake M, Kaneko H, Oshima H, Usui A, Ueda Y, Long-term results of tissue-engineered small-caliber vascular grafts in a rat carotid arterial replacement model, J. Artif. Organs 15(4) (2012) 399–405. [PubMed: 22806242]

[40]. Jacot JG, Abdullah I, Belkin M, Gerhard-Herman M, Gaccione P, Polak JF, Donaldson MC, Whittemore AD, Conte MS, Early adaptation of human lower extremity vein grafts: wall stiffness changes accompany geometric remodeling, J. Vase. Surg 39(3) (2004) 547–55.

[41]. Owens CD, Wake N, Jacot JG, Gerhard-Herman M, Gaccione P, Belkin M, Creager MA, Conte MS, Early biomechanical changes in lower extremity vein grafts--distinct temporal phases of remodeling and wall stiffness, J. Vase. Surg 44(4) (2006) 740–6.

[42]. Owens CD, Gasper WJ, Rahman AS, Conte MS, Vein graft failure, J. Vase. Surg 61(1) (2015) 203–16.

[43]. Dilley RJ, McGeachie JK, Tennant M, The role of cell proliferation and migration in the development of a neo-intimal layer in veins grafted into arteries, in rats, Cell Tissue Res 269(2) (1992) 281–7. [PubMed: 1423495]

[44]. Cooley BC, Murine model of neointimal formation and stenosis in vein grafts, Arterioscler. Thromb. Vase. Biol 24(7) (2004) 1180–5.

[45]. Wong AP, Nili N, Jackson ZS, Qiang B, Leong-Poi H, Jaffe R, Raanani E, Connelly PW, Sparkes JD, Strauss BH, Expansive remodeling in venous bypass grafts: novel implications for vein graft disease, Atherosclerosis 196(2) (2008) 580–9. [PubMed: 17692852]

[46]. Jiang Z, Tao M, Omalley KA, Wang D, Ozaki CK, Berceli SA, Established neointimal hyperplasia in vein grafts expands via TGF-beta-mediated progressive fibrosis, Am. J. Physiol. Heart Circ. Physiol 297(4) (2009) H1200–7. [PubMed: 19617405]

[47]. Wang J, Liu K, Shen L, Wu H, Jing H, Small interfering RNA to c-myc inhibits vein graft restenosis in a rat vein graft model, J. Surg. Res 169(1) (2011) e85–91. [PubMed: 21571310]

[48]. Tsou CL, Peters W, Si Y, Slaymaker S, Aslanian AM, Weisberg SP, Mack M, Charo IF, Critical roles for CCR2 and MCP-3 in monocyte mobilization from bone marrow and recruitment to inflammatory sites, J. Clin. Invest 117(4) (2007) 902–9. [PubMed: 17364026]

[49]. Gordon S, Taylor PR, Monocyte and macrophage heterogeneity, Nat. Rev. Immunol 5(12) (2005) 953–64. [PubMed: 16322748]

[50]. Willenborg S, Lucas T, van Loo G, Knipper JA, Krieg T, Haase I, Brachvogel B, Hammerschmidt M, Nagy A, Ferrara N, Pasparakis M, Eming SA, CCR2 recruits an inflammatory macrophage subpopulation critical for angiogenesis in tissue repair, Blood 120(3) (2012)613–25. [PubMed: 22577176]

[51]. Jiang Z, Yu P, Tao M, Ifantides C, Ozaki CK, Berceli SA, Interplay of CCR2 signaling and local shear force determines vein graft neointimal hyperplasia in vivo, FEBS Lett 583(21) (2009) 3536–40. [PubMed: 19822149]

[52]. Roh JD, Sawh-Martinez R, Brennan MP, Jay SM, Devine L, Rao DA, Yi T, Mirensky TL, Nalbandian A, Cidelsman B, Hibino N, Shinoka T, Saltzman WM, Snyder E, Kyriakides TR, Pober JS, Breuer CK, Tissue-engineered vascular grafts transform into mature blood vessels via an inflammation-mediated process of vascular remodeling, Proc. Natl. Acad. Sci. USA 107(10) (2010) 4669–74. [PubMed: 20207947]

[53]. Talacua H, Smits AI, Muylaert DE, van Rijswijk JW, Vink A, Verhaar MC, Driessen-Mol A, van Herwerden LA, Bouten CV, Kluin J, Baaijens FP, In Situ Tissue Engineering of Functional Small-Diameter Blood Vessels by Host Circulating Cells Only, Tissue Eng. Part A 21(19-20) (2015) 2583–94. [PubMed: 26200255]

[54]. Zhang X, Goncalves R, Mosser DM, The isolation and characterization of murine macrophages, Curr. Protoc. Immunol Chapter 14 (2008) Unit 14 1.

[55]. Davies LC, Jenkins SJ, Allen JE, Taylor PR, Tissue-resident macrophages, Nat. Immunol 14(10) (2013) 986–95. [PubMed: 24048120]

[56]. Syedain ZH, Meier LA, Lahti MT, Johnson SL, Tranquillo RT, Implantation of completely biological engineered grafts following decellularization into the sheep femoral artery, Tissue Eng. Part A 20(11-12) (2014) 1726–34. [PubMed: 24417686]

[57]. Koobatian MT, Row S, Smith RJ Jr., Koenigsknecht C, Andreadis ST, Swartz DD, Successful endothelialization and remodeling of a cell-free small-diameter arterial graft in a large animal model, Biomaterials 76 (2016) 344–58. [PubMed: 26561932]

[58]. Roach MR, Burton AC, The reason for the shape of the distensibility curves of arteries, Can. J. Biochem. Physiol 35(8) (1957) 681–90. [PubMed: 13460788]

[59]. Hill MR, Duan X, Gibson GA, Watkins S, Robertson AM, A theoretical and non-destructive experimental approach for direct inclusion of measured collagen orientation and recruitment into mechanical models of the artery wall, J. Biomech 45(5) (2012) 762–71. [PubMed: 22305290]

[60]. Gathercole LJ, Keller A, Early Development of Crimping in Rat Tail Tendon Collagen - Polarizing Optical and Sem Study, Micron 9(2) (1978) 83–89.

[61]. Holzapfel GA, Gasser TC, Ogden RW, A new constitutive framework for arterial wall mechanics and a comparative study of material models, Journal of Elasticity 61(1-3) (2000) 1–48.

[62]. Wagenseil JE, Mecham RP, Vascular extracellular matrix and arterial mechanics, Physiol. Rev 89(3) (2009) 957–89. [PubMed: 19584318]

[63]. Corr DT, Hart DA, Biomechanics of Scar Tissue and Uninjured Skin, Adv. Wound Care 2(2) (2013)37–43.

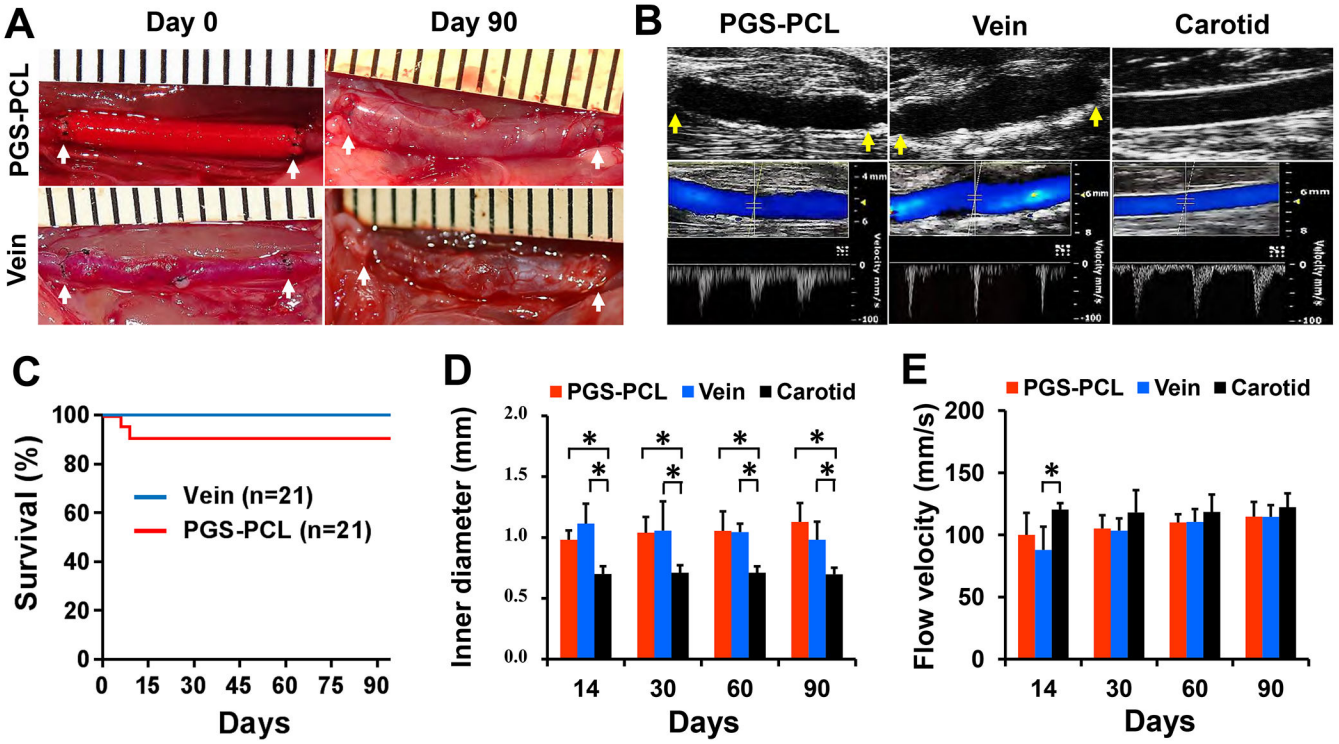

Fig.1. Graft implantation and patency.

(A) Gross appearance of the grafts at day 0 and 90 post-implantation. Arrows indicate suture lines. PGS-PCL, synthetic graft. Vein, vein graft. (B) Representative ultrasound images of grafts and native artery at day 90. B-mode (top row), color Doppler and pulse wave (PW) modes (bottom row). Arrows indicate suture lines. Carotid, native common carotid artery. (C) Survival plot showing the overall patency of the grafts. There is no statistical difference between two grafts ($P = 0.15$). (D) The inner diameter measured by B-mode images. (E) Flow velocity measured in the middle region of the grafts and native carotids by PW mode images. Data in (D) and (E) are means ± standard deviation (SD) ($n = 5$). * represents $P < 0.05$.

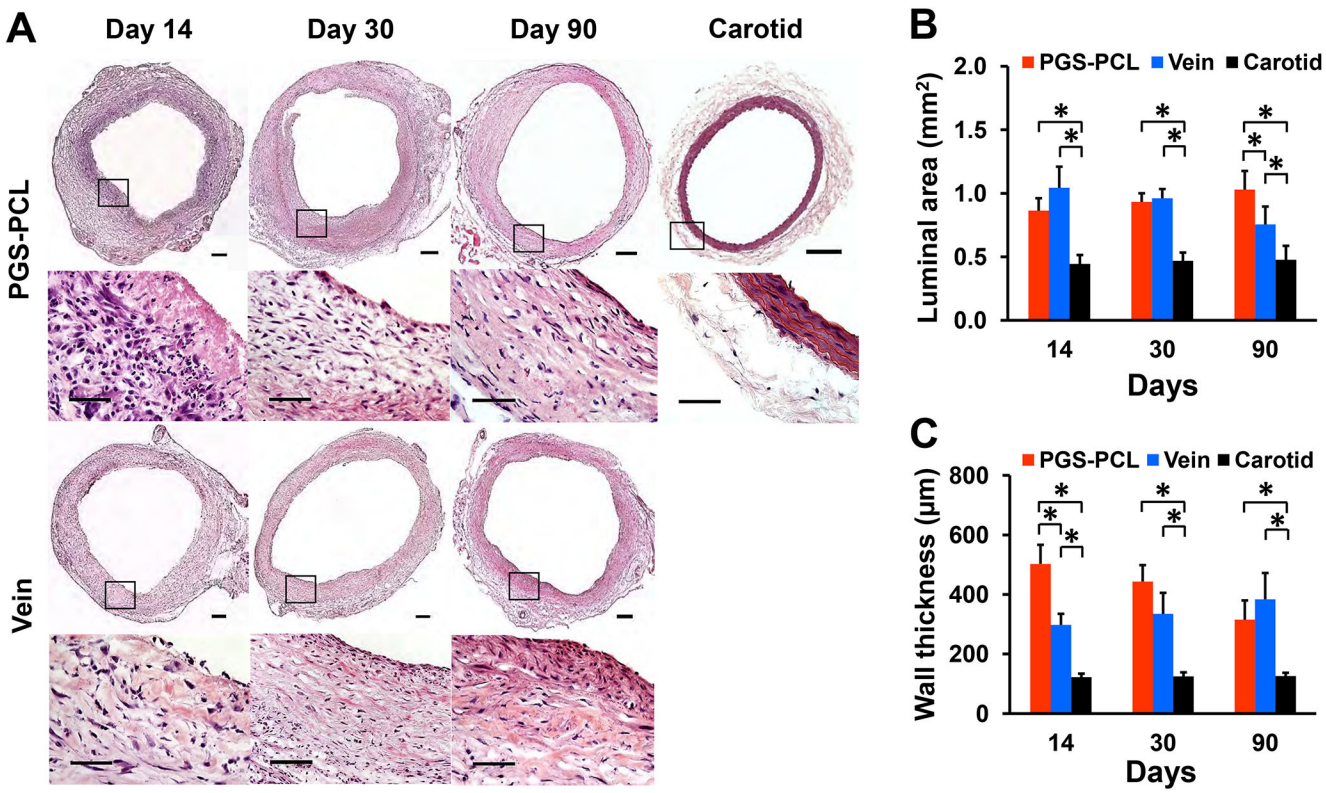

Fig.2. Histological and morphological assessments at middle regions.

(A) Representative images for H&E staining in the middle region of grafts and native carotids at each time point. The bottom row represents the magnification of the box region shown in the top row. Scale bars, 200 μm (top row) and 50 μm (bottom row). (B) Luminal area. (C) Wall thickness. Both (B) and (C) were measured by using H&E stained images from three independent sections per sample. Data in (B) and (C) are means ± SD ($n = 4$). * represents $P < 0.05$.

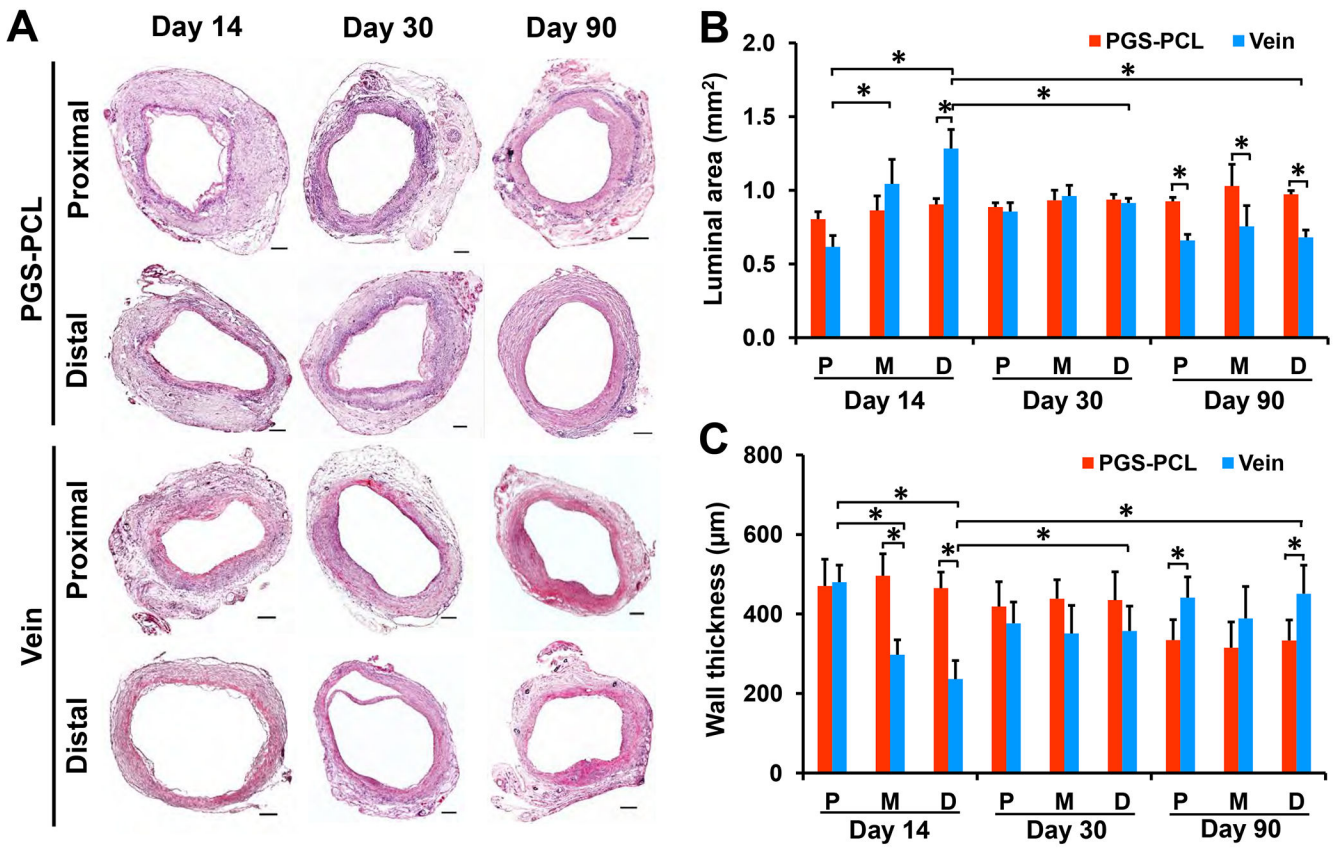

Fig.3. Histological and morphological assessments of grafts at anastomotic regions.

(A) Representative images for H&E staining in both proximal and distal regions of grafts at each time point. Scale bars, 200 μm. (B) Luminal area. (C) Wall thickness. P, proximal. M, middle. D, distal. Both (B) and (C) were measured by using H&E stained images from three independent sections per sample. Data in (B) and (C) are means ± SD ($n = 4$). * represents $P < 0.05$.

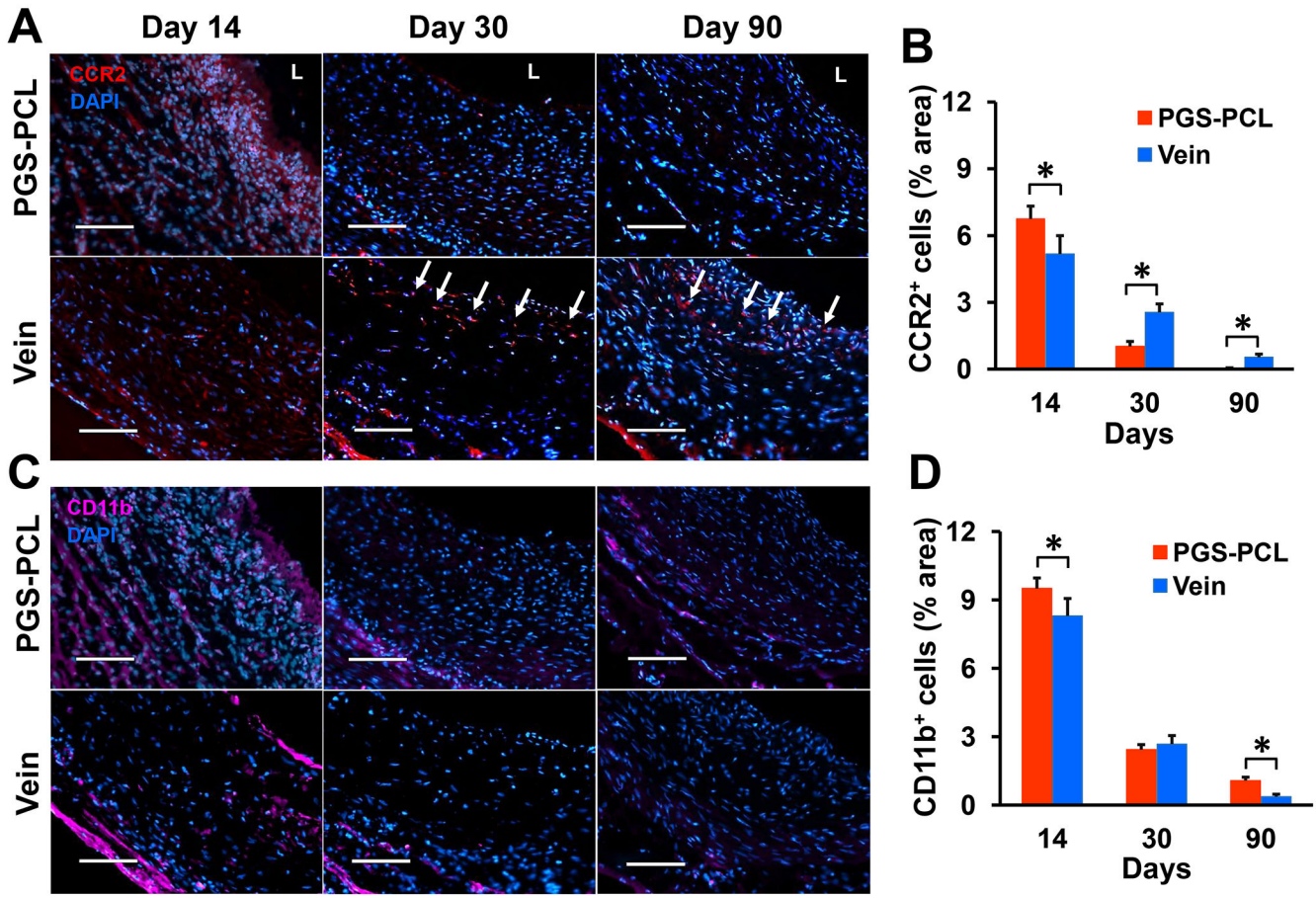

Fig.4. Infiltration of inflammatory monocytes.

(A) Representative images for immunofluorescence staining with the monocyte recruitment marker CCR2. Arrows denote $CCR2^+$ cells. L, lumen. (B) Quantification of the results shown in (A). (C) Representative images for immunofluorescence staining with the monocyte adhesion, migration marker CD11b. (D) Quantification of the results shown in (C). Scale bars, 100 μm (A and C). Data in (B) and (D) are means ± SD ($n = 4$). * represents $P < 0.05$.

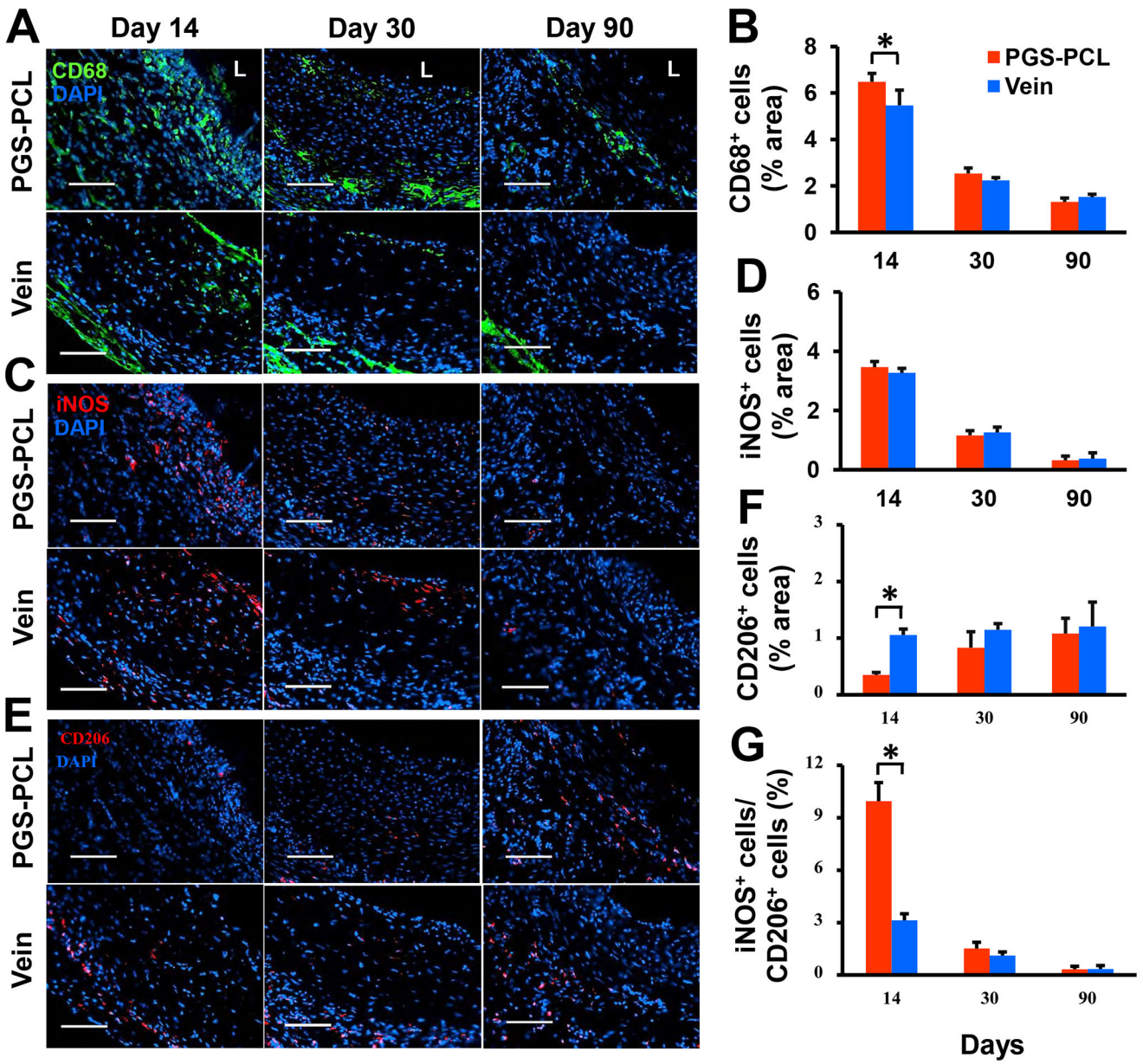

Fig.5. Macrophage infiltration and polarization.

(A) Representative images for immunofluorescence staining with the pan-macrophage marker CD68. L, lumen. (B) Quantification of the results shown in (A). (C) Representative images for immunofluorescence staining with the Ml macrophage marker iNOS. (D) Quantification of the results shown in (C). (E) Representative images for immunofluorescence staining with the M2 macrophage marker CD206. (F) Quantification of the results shown in (E). (G) The area ratio of $iNOS^+$ to $CD206^+$ cells representing the M1/M2 macrophage ratio. Scale bars, 100 μm (A, C, and E). Data in (B), (D), (F) and (G) are means ± SD ($n = 4$). * represents $P < 0.05$.

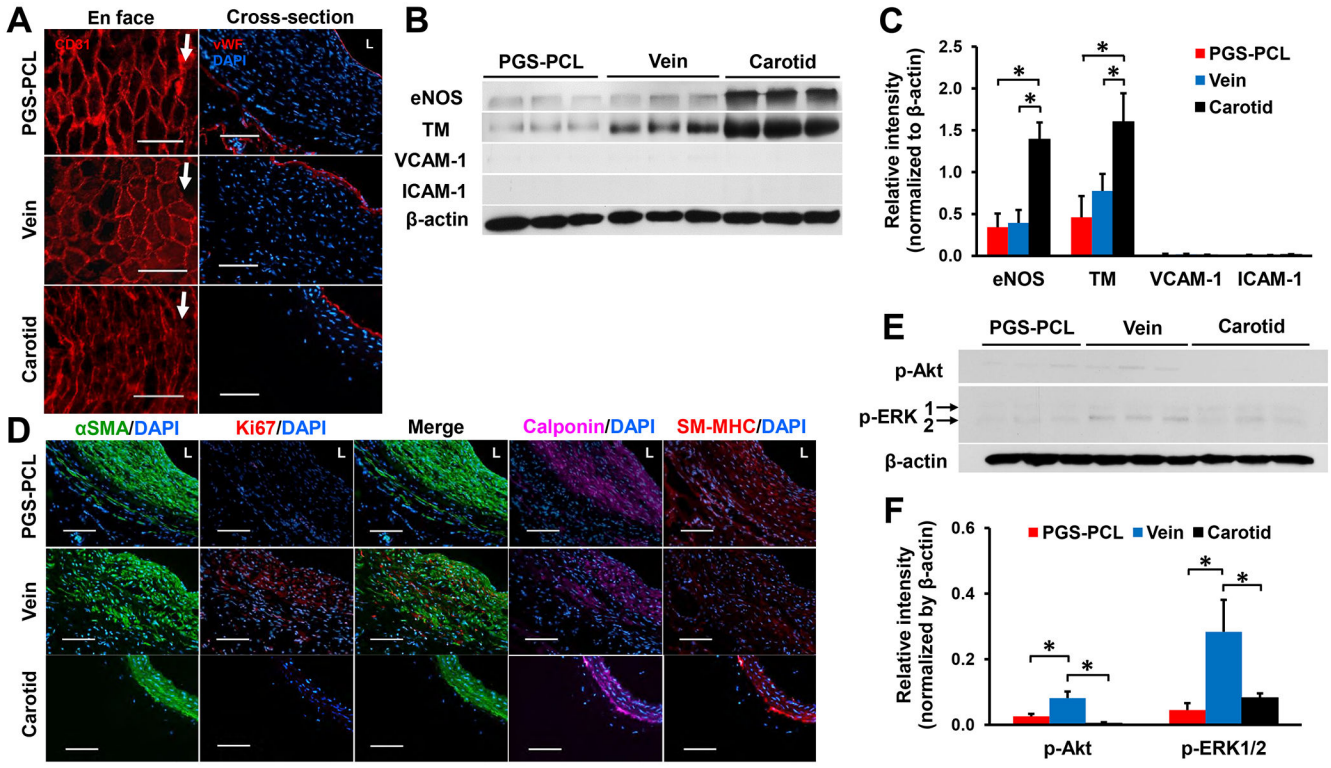

Fig.6. Arterial-like tissue remodeling at day 90.

(A) Representative images for en face (left) and cross-sectional (right) immunofluorescence staining with EC markers, CD31 and vWF. Arrows indicated the flow direction. L, lumen. Scale bars, 100 μm. (B) Immunoblots of grafts and native carotids for eNOS, TM, VCAM-1, and ICAM-1. (C) Quantification of the relative intensity of each blot normalized to β-actin expression. Data are means ± SD ($n = 3$). * represents $P < 0.05$. (D) Representative images for immunofluorescence staining with SMC phenotype markers, αSMA, calponin, and smooth muscle-myosin heavy chain (SM-MHC), and proliferation marker Ki67. L, lumen. Scale bars, 100 μm. (E) Immunoblots of p-Akt (Ser473) and p-ERK1/2. p-ERK1, 44 kDa (top). p-ERK2, 42 kDa (bottom). (F) Quantification of the relative intensity of each blot normalized to β-actin expression. Data are means ± SD ($n = 3$). * represents $P < 0.05$.

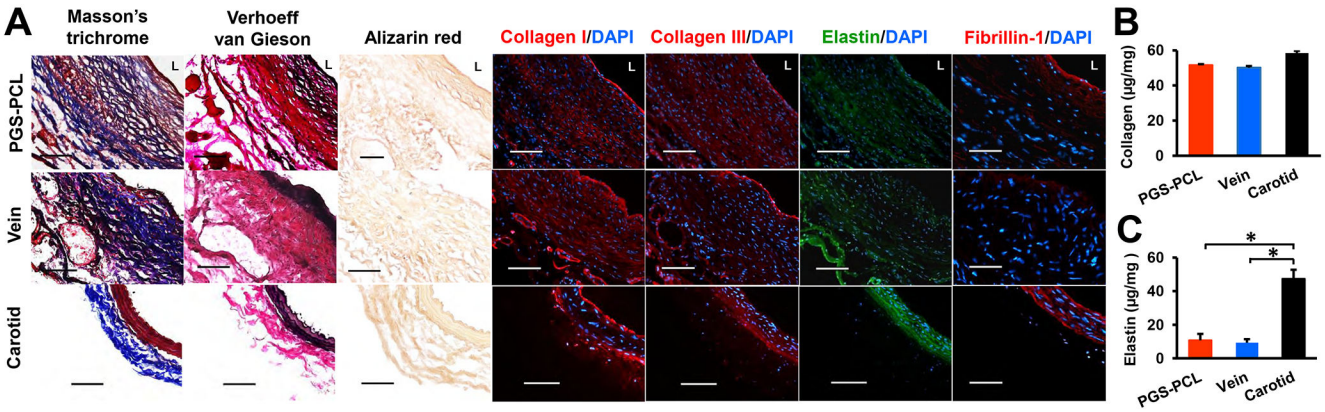

Fig.7. ECM protein deposition and quantification at day 90.

(A) Representative images for histology and immunofluorescence staining with collagen and elastin markers. Masson's trichrome, Verhoeff-van Gieson, Alizarin red staining show collagen (blue), elastin (black), but no calcium (red) deposition, respectively. L, lumen. Scale bars, 100 μm. (B) Quantification of total collagen using Sircol Insoluble Collagen assay. (C) Quantification of elastin using Fastin assay. Data in (B) and (C) are means ± SD ($n = 4$). * represents $P < 0.05$.

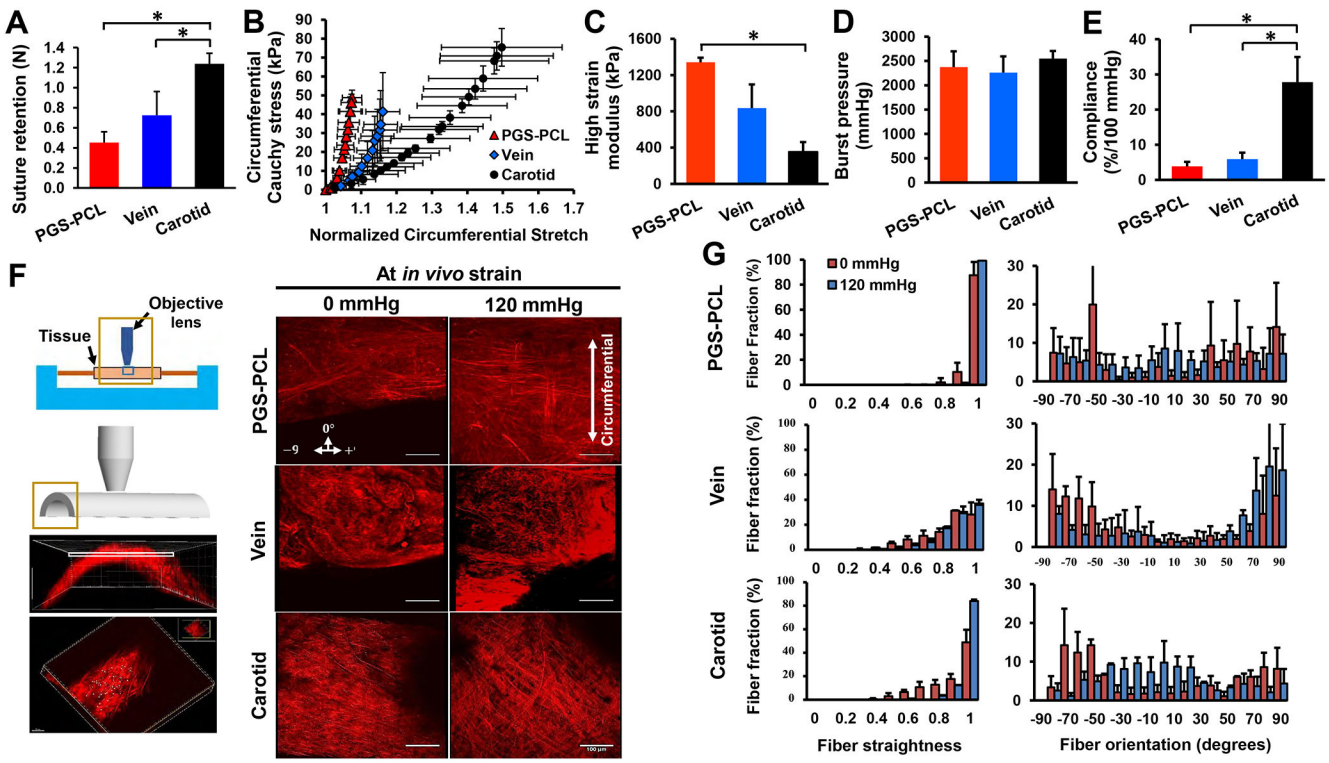

Fig.8. Assessment of mechanical response.

(A) Suture retention strength of bare grafts and native vessels before implantation. (B) Circumferential stress-stretch curves. (C) High strain moduli. (D) Burst pressure. (E) Compliance. (F) Schematic of biaxial inflation device used with a multiphoton microscope to image collagen fibers (left). Planar images were obtained starting from the outer wall, moving down to the inner wall with images stacked to obtain projection images of collagen fibers across the thickness of the sample. Scale bars, 100 μm. Note the difference in collagen fiber density, morphology and orientation between samples (right). (G) Collagen fiber straightness and orientation quantified in each slice across sample thickness and normalized to a total number of traced fibers. A value of 1 represents completely straightened (recruited) fibers. Orientation was measured from $\theta = 0°$ to 90° with $\theta = 0°$ being the circumferential direction. Data in (A) - (E) are means ± SD ($n = 5$ for A and $n = 3$ for B - E). Data in (B)-(G) were obtained from explanted grafts and native carotids at day 90. * represents $P < 0.05$.